

High-Speed Trains Access Connectivity Through RIS-Assisted FSO Communications

Pouya Agheli, Hamzeh Beyranvand, and Mohammad Javad Emadi

Abstract—Free-space optic (FSO) is a promising solution to provide broadband Internet access for high-speed trains (HSTs). Besides, reconfigurable intelligent surfaces (RIS) are considered as hardware technology to improve performance of optical wireless communication systems. In this paper, we propose a RIS-assisted FSO system to provide access connectivity for HTSs, as an upgrade for the existing direct and relay-assisted FSO access setups. Our motivation is mainly based on well-proven results indicating that a RIS-assisted optical wireless system, with a large enough number of RIS elements, outperforms a relay-assisted one thanks to its programmable structure. We firstly compute the statistical expressions of the considered RIS-assisted FSO channels under weak and moderate-to-strong fading conditions. Then, the network's average signal-to-noise ratio and outage probability are formulated based on the assumed fading conditions, and for two fixed- and dynamic-oriented RIS coverage scenarios. Our results reveal that the proposed access network offers up to around 44% higher data rates and 240% wider coverage area for each FSO base station (FSO-BS) compared to those of the relay-assisted one. The increase of coverage area, on average, reduces 67% the number of required FSO-BSs for a given distance, which results in fewer handover processes compared to the alternative setups. Finally, the results are verified through Monte-Carlo simulations.

Index Terms—Free-space optic, high-speed trains, reconfigurable intelligent surfaces, access network, average signal-to-noise ratio, and outage probability.

I. INTRODUCTION

THE drastic increase of Internet-based applications and video on demand streaming along with the growing interest in high-speed trains (HSTs), has created a popular research topic on providing seamless high-capacity access networks for HSTs. The main objective is to ensure high quality of service (QoS), i.e., high data rates and low latency, for the passengers in an HST similar to generic pedestrian users despite the train's high speed of up to 500 [km/h] [1]. Indeed, we must propose a reliable access network, to not only enables high-rate communications but also results in low handover frequency [2]. To achieve this goal, multiple radio and optical wireless technologies with different setups have been utilized since the first launch of HSTs [1]–[17]. The well-known wireless access solutions for HSTs, such as the global system for mobile communications-railway (GSM-R) [5], long-term evolution for railways (LTE-R) [6], dual-hop worldwide interoperability for microwave access (WiMAX) [7], and dual-hop mobile broadband wireless access (MBWA) [8], have been deployed in several countries. However, these

technologies cannot ensure high QoS for upcoming HSTs in the presence of rapidly time-varying and non-stationary wireless channels, co-channel interference, high path-loss attenuation for millimeter-wave and terahertz bands, high handover frequency, and strong Doppler shifts [3], [4]. To address some fundamental challenges of the proposed radio technologies for HSTs, *free-space optic* (FSO) has gained research attention, as discussed in [2], [3], and [9]–[17].

The FSO technology offers high capacity with rapid setup time, easy upgrade, flexibility, freedom from spectrum license regulations, and enhanced security [18]. However, it comes at the expense of some drawbacks such as pointing error, line-of-sight connectivity requirement, and sensitivity to atmospheric conditions [19]–[22]. The FSO channel modeling in HSTs is faced with some challenges by reason of unsteady environmental differences, such as tunnels, hills, and dense areas. In this case, an analytical study on ground-to-train channel modeling for typical FSO links has been performed in [9]. An experimental prototype for the demonstration of ground-to-train FSO communications has been also presented in [10]. Due to the large divergence angles of FSO beams for HST systems and as a result severe distance-dependent beam spreading, each FSO base station (FSO-BS) serves only a narrow region. Thus, we face some challenges such as demanding a large number of FSO-BSs, frequent handovers, and high capital expenditures (CAPEX) to provide seamless coverage, [2] and [11]–[14].

Han et al. [11] have proposed a radio-over-fiber setup as antenna extender (RADIATE) solution to address the frequent handover and rapid channel variation issues. This solution provides broadband Internet services for HSTs with cellular backhaul networks. The authors of [12] have utilized the advantages of the RADIATE solution and proposed an FSO-based communication technology for HSTs, referred to as free-space optic utilization in high-speed trains (FOCUS). The FOCUS solution reduces frequent handovers, prevents handoff congestion, balances the traffic load among transceivers, and handles fast channel variations in HST communications. In addition, Fan et al. [13] have exploited the dual transceivers scheme in a ground-to-train communications system, where two transceivers of an FSO-BS can point to different directions. Thanks to this scheme, two transceivers at the front- and back-end of HST can cooperate to maintain continuous ground-to-train FSO communications. Therefore, the number of FSO-BSs decreases and the impacts of frequent handovers are alleviated. The same authors have also suggested a rotating transceiver scheme to mitigate the impacts of handover processes via utilizing steerable FSO transceivers for HST

The authors are with the Department of Electrical Engineering, Amirkabir University of Technology (Tehran Polytechnic), Tehran 1591634311, Iran (E-mails: {pouya.agheli, beyranvand, mj.emadi}@aut.ac.ir).

communications, as in [14]. Moreover, as an attempt to provide seamless FSO communications for next-generation HSTs, optimal positions of FSO-BSs have been found in [2] under two single- and dual-wavelength FSO coverage models.

In order to decrease the number of FSO-BSs and handover processes, an interesting solution is to take advantage of relay-assisted transmissions for FSO links. In this regard, multi-hop short-length FSO links would experience better conditions compared to that of the direct transmissions [23]. Thus, each FSO-BS with its paired relay can support a wider area. To choose an appropriate relaying model, it has been shown that all-optical relaying offers a favorable trade-off between complexity and performance, and it is considered as a low-complexity solution [24]. Most recently, it has been shown that UAV-based FSO air-relay systems provide wider coverage areas for HSTs compared to conventional ground-relay ones [3]. The UAV-assisted air-relay systems for HSTs were firstly introduced in [25], where a flying UAV relays data between a moving train car and a network gateway. Even though the air-relay systems perform better than the fixed ground-relay systems, it is not affordable and optimal to build a UAV swarm over a moving train to provide Internet access for the train's passengers in non-emergency conditions.

Recently, *reconfigurable intelligent surfaces* (RISs) have been defined as hardware technology to improve the performances of wireless and optical wireless systems [26]–[29]. The fundamental features and channel modeling of RIS-assisted optical wireless systems have been widely studied in the literature, e.g., [27], [28], and [30]–[35], under different physical conditions. It is well known that we can use two different types of optical RIS structures for deploying a RIS-assisted optical wireless system; *metasurfaces* and *mirror arrays* [34]. These structures can be based on integrated seamless surfaces or hundreds of micro-mirrors built with micro-electromechanical systems (MEMS). In dual-hop FSO systems, the RIS technology can gather dispersed beams and reconfigure them through desired directions, whereas the relay systems can only reflect a portion of the incident FSO beams and disregards the rest. Indeed, it has been proven that RIS-assisted systems, with a large enough number of elements, outperform the relay ones for wireless transmissions [36] and [37]. The results can be extended for optical wireless transmissions. According to the mentioned factors, the RIS technology can add novelty to the existing direct or relay-assisted FSO access networks for HSTs and be considered as a promising solution to decrease the number of required FSO-BSs for a given distance. In this paper, we analyze a RIS-assisted FSO system to provide an access network for an HST, which has not been studied to the best of our knowledge. In summary, the key contributions of the paper are as follows.

- Deriving the channel probability distribution function (p.d.f) of the proposed RIS-assisted FSO system under weak and moderate-to-strong fading conditions.
- Formulating the average signal-to-noise ratio (SNR) and closed-form outage probability expressions under the assumed fading conditions and considering two scenarios for RIS coverage; fixed- and dynamic-oriented ones.
- Evaluating the proposed system's performance through

Monte-Carlo simulations and analytical results. Furthermore, it is shown that the proposed access network not only increases the achievable data rates at the HST but also boosts the coverage area supported by each FSO-BS and its paired RIS compared to those of the relay-assisted alternatives. Also, our proposed system results in lower number of FSO-BSs, handover processes, and CAPEX.

- Presenting a system design framework for practical deployments.

Organization: Section II introduces the proposed RIS-assisted FSO system. The network's performance metrics are derived in Section III. Numerical results and discussions in addition to the system design framework are presented in Section IV. Finally, the paper is concluded in Section V.

Notation: $\Gamma(\cdot)$ and $\Gamma(s, x) = \int_x^\infty t^{s-1} e^{-t} dt$ sequentially denote the Gamma and upper incomplete Gamma functions. $K_\alpha(\cdot)$ is the modified Bessel function of the second kind. Also, $\text{erf}(x) = \frac{2}{\sqrt{\pi}} \int_0^x e^{-t^2} dt$ and $\text{erfc}(x) = 1 - \text{erf}(x)$ indicate the error and complementary error functions, respectively. Besides, $\mathbb{E}\{\cdot\}$ is the statistical expectation, and $z \sim \mathcal{N}(m, \sigma^2)$ shows real-valued symmetric Gaussian random variable with mean m and variance σ^2 . Moreover, $\mathbb{I}(\mathcal{C})$ denotes an indicator function, where $\mathbb{I}(\mathcal{C}) = 1$ if the condition \mathcal{C} is satisfied, and $\mathbb{I}(\mathcal{C}) = 0$, otherwise. Finally, $G_{p,q}^{m,n}(z |_{b_1, b_2, \dots, b_q}^{a_1, a_2, \dots, a_p})$ presents the Meijer's G-function.

II. SYSTEM MODEL

We assume a RIS-assisted FSO access network in which B FSO-BSs and R RISs cooperatively serve an HST system, c.f. Fig. 1. In this setup, at each time, the HST is served via either a *direct* FSO beam transmitted from an FSO-BS or *RIS-assisted* FSO beams reflected from a RIS. Each train car is equipped with an avalanche photodetector placed on its roof, which delivers the gathered data from outside to an intra-train network. In Fig. 1, L_b , for $b = 1, 2, \dots, B$, and L_m denote the lengths of the regions covered by direct and RIS-assisted FSO beams, respectively. In addition, L_d and L_0 indicate the vertical and horizontal distances of every FSO-BS from the track, respectively. Furthermore, the FSO beam expander at each FSO-BS adjusts its divergence angle to cover the whole area of the paired RIS. Each RIS consists of N_m cells, as shown in Fig. 2, where each cell provides a concentrated beam by its $N_k \times N_\ell$ micro-mirror elements. Given that, we consider two coverage strategies based on the RIS-assisted FSO beams; fixed-oriented reflection (FOR) and dynamic-oriented reflection (DOR). In the FOR scenario, the coverage area L_m is divided into N_m one-dimensional grids, where each one is independently covered by a single RIS cell's beam under a fixed orientation. However, in the DOR case, all cells dynamically point their beams to the HST's detector and all them serve the HST simultaneously. In this case, train tracking is required to contrast probable FSO misalignments. As shown in Fig. 1, RIS_r paired with FSO-BS_b and RIS_{r+1} paired with FSO-BS_{b+1} , for $r = 1, 2, \dots, R$, where RIS_r and RIS_{r+1} work based on the FOR and DOR strategies, respectively.

Before analyzing the network's performance, in what follows, we model the RIS-assisted and direct FSO channels, then we present the received signals at the HST's detector.

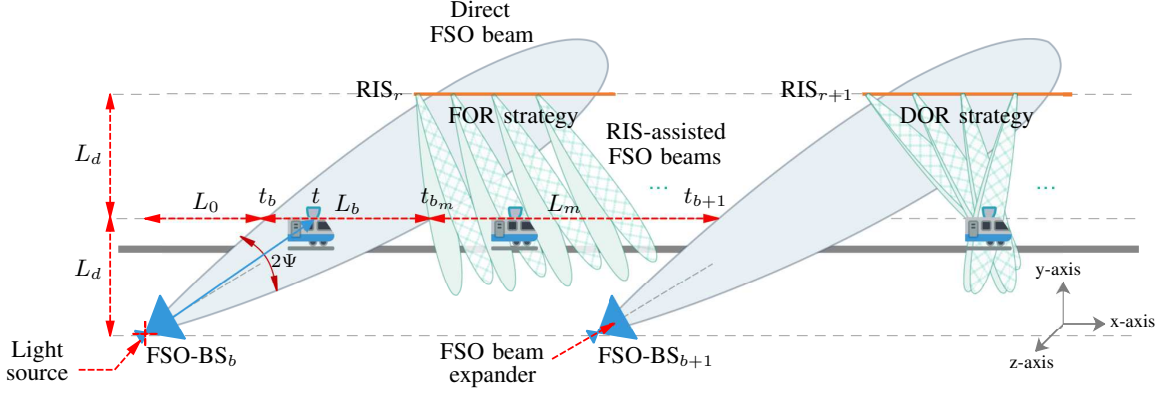


Fig. 1. The RIS-assisted FSO access network serving an HST system.

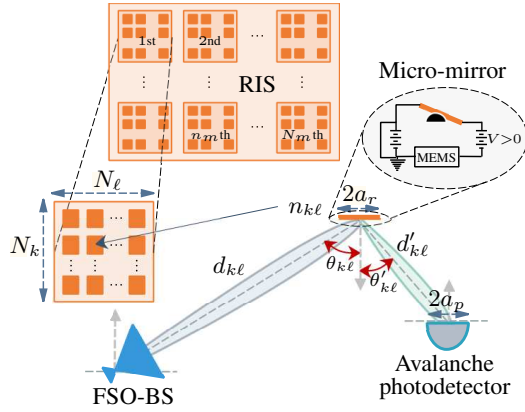


Fig. 2. The FSO beam's reflection through a RIS-assisted structure.

A. RIS-Assisted FSO Channel Model

An end-to-end FSO channel between any FSO-BS and the HST's detector, which is assisted via the $n_{k\ell}$ th element of the RIS, as depicted in Fig. 2, is modeled by $h_{k\ell} = h_{p,k\ell} h_{t,k\ell} h_{g,k\ell}$. Here, $h_{p,k\ell}$, $h_{t,k\ell}$, and $h_{g,k\ell}$ denote the path-loss, turbulence-induced fading, and the sum of geometric and misalignment losses (GML), respectively, which are discussed as follows.

1) *Path-Loss*: Under the Beer's law, $h_{p,k\ell}$ is given by

$$h_{p,k\ell} = 10^{-\gamma d_{e,k\ell}}, \quad (1)$$

where γ and $d_{e,k\ell} = d_{k\ell} + d'_{k\ell}$ present the attenuation factor and end-to-end distance, respectively.

2) *Turbulence-Induced Fading*: The distribution of $h_{t,k\ell}$ is log-normal, i.e., $h_{t,k\ell} \sim \text{LN}(\mu_{k\ell}, \sigma_{k\ell}^2)$, or Gamma-Gamma, i.e., $h_{t,k\ell} \sim \text{GG}(\alpha_{k\ell}, \beta_{k\ell})$, under weak or moderate-to-strong turbulence condition, sequentially. Hence, we have [19], [20]

$$f_{h_{t,k\ell}}(h_{t,k\ell}) = \begin{cases} \frac{1}{h_{t,k\ell} \sqrt{8\pi\sigma_{k\ell}^2}} \exp\left(-\frac{(\ln(h_{t,k\ell}) - 2\mu_{k\ell})^2}{8\sigma_{k\ell}^2}\right), & \text{for LN,} \\ \frac{2(\alpha_{k\ell}\beta_{k\ell}h_{t,k\ell})^{\frac{\alpha_{k\ell}+\beta_{k\ell}}{2}}}{\Gamma(\alpha_{k\ell})\Gamma(\beta_{k\ell})h_{t,k\ell}} K_{\alpha_{k\ell}-\beta_{k\ell}}\left(2\sqrt{\alpha_{k\ell}\beta_{k\ell}}h_{t,k\ell}\right), & \text{for GG,} \end{cases} \quad (2)$$

where $\mu_{k\ell} = -\sigma_{k\ell}^2$, $\sigma_{k\ell}^2 = 0.307C_n^2 k^{7/6} d_{e,k\ell}^{11/6}$, C_n^2 represents the refractive structure's index, $k = 2\pi/\lambda$ is the optical wave number, and λ denotes the wavelength. Also, we have [19]

$$\alpha_{k\ell} = \left[\exp\left(\frac{1.96\sigma_{k\ell}^2}{(1+4.44\sigma_{k\ell}^{12/5})^{7/6}}\right) - 1 \right]^{-1}, \quad (3a)$$

$$\beta_{k\ell} = \left[\exp\left(\frac{2.04\sigma_{k\ell}^2}{(1+2.76\sigma_{k\ell}^{12/5})^{5/6}}\right) - 1 \right]^{-1}. \quad (3b)$$

3) *GML*: Given the positions and orientations of the assumed FSO-BS, RIS, and HST's detector, the conditional GML is given by the following p.d.f [28]

$$f_{h_{g,k\ell}}(h_{g,k\ell}) = \frac{\sqrt{\varpi_{k\ell}}}{2\sqrt{\pi}h_{0,k\ell}} \left[\ln\left(\frac{h_{0,k\ell}}{h_{g,k\ell}}\right) \right]^{-1/2} \left(\frac{h_{g,k\ell}}{h_{0,k\ell}}\right)^{\varpi_{k\ell}-1}, \quad (4)$$

if $0 \leq h_{g,k\ell} \leq h_{0,k\ell}$, where $h_{0,k\ell} = \text{erf}(v_{k\ell})$, $v_{k\ell} = \sqrt{2} \cos(\theta'_{k\ell}) w^{-1}(d_{e,k\ell}, \hat{w}_0) a_p$, and we have

$$w(d_{e,k\ell}, \hat{w}_0) = \hat{w}_0 \sqrt{1 + \left(\frac{\lambda d_{e,k\ell}}{\pi \hat{w}_0^2}\right)^2}, \quad (5a)$$

$$\varpi_{k\ell} = \frac{\sqrt{\pi}}{8} \frac{h_{0,k\ell} w^2(d_{e,k\ell}, \hat{w}_0)}{v_{k\ell} \exp(-v_{k\ell}^2) \cos^2(\theta'_{k\ell}) \delta_m^2}, \quad (5b)$$

$$\delta_m^2 = \frac{1}{\cos^2(\theta'_{k\ell})} \left(\frac{\cos^2(\theta'_{k\ell})}{\cos^2(\theta_{k\ell})} \delta_s^2 + \frac{\sin^2(\theta_{k\ell} + \theta'_{k\ell})}{\cos^2(\theta_{k\ell})} \delta_r^2 + \delta_l^2 \right). \quad (5c)$$

In (5c), δ_s^2 , δ_r^2 , and δ_l^2 denote variances of building sway fluctuations at the FSO-BS, RIS, and detector, respectively [28]. By using (1), (2), and (4), the p.d.f.s of $h_{k\ell}$ for the two turbulence conditions are computed in the subsequent theorems.

Theorem 1. The p.d.f of $h_{k\ell}$ under the weak turbulence is

$$f_{h_{k\ell}}(h_{k\ell}) = \frac{\sqrt{\varpi_{k\ell}}}{8\sqrt{\pi}} \left(\frac{h_{k\ell}}{C_a}\right)^{\varpi_{k\ell}} \text{erfc}\left(\frac{\ln\left(\frac{h_{k\ell}}{C_a}\right) + C_b}{\sqrt{8\sigma_{k\ell}^2}}\right) \times \left\{ \left[\frac{5 - \ln(C_a)}{h_{k\ell}^{\varpi_{k\ell}}} + \frac{\sqrt{8\sigma_{k\ell}^2}}{\sqrt{\pi}} \right] \times \exp\left(\frac{(\ln(h_{k\ell}) + C_b)^2 - (\ln(h_{k\ell}) + 2\sigma_{k\ell}^2)^2}{8\sigma_{k\ell}^2}\right) \right\}$$

$$+ (\ln(h_{k\ell}) + C_b) \exp\left(2\sigma_{k\ell}^2 \varpi_{k\ell}(1 + \varpi_{k\ell})\right)\Bigg\}, \quad (6)$$

where $C_a = h_{0,k\ell} h_{p,k\ell}$, and $C_b = 2\sigma_{k\ell}^2(1 + 2\varpi_{k\ell})$.

Proof. See Appendix A.

Theorem 2. The p.d.f of $h_{k\ell}$ under the moderate-to-strong turbulence becomes

$$f_{h_{k\ell}}(h_{k\ell}) = \frac{\sqrt{\varpi_{k\ell}\zeta}}{2\sqrt{\pi}\Gamma(\alpha_{k\ell})\Gamma(\beta_{k\ell})} \frac{1}{h_{k\ell}} \left(\frac{\alpha_{k\ell}\beta_{k\ell}h_{k\ell}}{C_a}\right)^{C_c} \times G_{1,3}^{3,0}\left(\frac{\alpha_{k\ell}\beta_{k\ell}h_{k\ell}}{C_a} \middle| \begin{matrix} 1+\varpi_{k\ell} \\ 1+C_c, \alpha_{k\ell}, \beta_{k\ell} \end{matrix}\right), \quad (7)$$

where $C_c = 1/2\zeta + \varpi_{k\ell} - 1$.

Proof. See Appendix B.

B. Direct FSO Channel Model

The direct FSO channel between the b th FSO-BS and the HST's detector at time $t_b \leq t \leq t_{b_m}$ is modeled as $h_b(t) = h_{p,b}(t)h_{t,b}(t)h_{g,b}(t)$ in which $h_{p,b}(t) = 10^{-\gamma d_b(t)}$, and

$$d_b(t) = \sqrt{L_d^2 + (L_0 + (t - t_b)V_{\text{HST}})^2}, \quad (8)$$

where V_{HST} denotes the HST's speed. For modeling the path-loss and turbulence-induced fading, the same formulas as in (2) and (3) are used, where $h_{t,k\ell}$, $\mu_{k\ell}$, $\sigma_{k\ell}^2$, $\alpha_{k\ell}$, $\beta_{k\ell}$, $d_{e,k\ell}$ are replaced with $h_{t,b}(t)$, μ_b , σ_b^2 , α_b , β_b , $d_b(t)$, sequentially. Also, the GML reduces to the misalignment loss modeled as [20]

$$f_{h_{g,b}(t)}(h_{g,b}(t)) = \frac{\xi^2}{h_{0,b}^{\xi^2}} (h_{g,p}(t))^{\xi^2-1}, \text{ for } 0 \leq h_{g,b}(t) \leq h_{0,b}, \quad (9)$$

where $h_{0,b}$ and ξ denote misalignment parameters. Thus, the p.d.f of $h_b(t)$ under the weak turbulence is given by [38]

$$f_{h_b(t)}(h_b(t)) = \frac{\xi^2(h_b(t))^{\xi^2-1}}{2C_d^{\xi^2}} \operatorname{erfc}\left(\frac{\ln\left(\frac{h_b(t)}{C_d}\right) + C_e}{\sqrt{8\sigma_b^2}}\right) C_f, \quad (10)$$

where $\sigma_b^2 = 0.307C_n^2 k^{7/6}(d_b(t))^{11/6}$, $C_d = h_{0,b}h_{p,b}(t)$, $C_e = 2\sigma_b^2(1 + 2\xi^2)$, and $C_f = 2\sigma_b^2\xi^2(1 + \xi^2)$. The p.d.f of $h_b(t)$ under the moderate-to-strong turbulence is derived in the following theorem.

Theorem 3. The p.d.f of $h_b(t)$ under the moderate-to-strong turbulence is

$$f_{h_b(t)}(h_b(t)) = \frac{\xi^2}{\Gamma(\alpha_b)\Gamma(\beta_b)} \frac{1}{h_b(t)} \left(\frac{\alpha_b\beta_b h_b(t)}{C_d}\right)^{\xi^2} \times G_{1,3}^{3,0}\left(\frac{\alpha_b\beta_b h_b(t)}{C_d} \middle| \begin{matrix} 1+\xi^2 \\ \xi^2, \alpha_b, \beta_b \end{matrix}\right). \quad (11)$$

Proof. See Appendix C.

C. HST Received Signals

In this section, we model the FSO received signals at the HST's detector for the FOR and DOR strategies. To this end, we recall $h_{k\ell}$ as $h_{m,k\ell}$ with similar properties and dedicated to the n_m RIS cell, for $n_m = 1, 2, \dots, N_m$. Let us assume

an intensity modulation/direct detection (IM/DD) FSO system, where $s_b(t) \in \{0, \sqrt{P}\}$ denotes the transmitted symbol from the b th FSO-BS at time t . According to Fig. 1, the HST's detector receives the signal from the b th FSO-BS via direct FSO channels if $t_b \leq t < t_{b_m}$ and via RIS-assisted ones if $t_{b_m} \leq t < t_{b+1}$. Therefore, the received signal is modeled as¹

$$r_b(t) = \begin{cases} (\eta h_b(t)s_b(t) + \omega(t))\mathbb{I}(\mathcal{C}_1), \\ \text{FOR: } \left\{ \eta \left(\sum_{\ell=1}^{N_\ell} \sum_{k=1}^{N_k} \rho_{k\ell} h_{m,k\ell} \right) s_b(t) + \omega'(t) \right\} \mathbb{I}(\mathcal{C}_2), \\ \text{DOR: } \left\{ \eta \left(\sum_{n_m=1}^{N_m} \sum_{\ell=1}^{N_\ell} \sum_{k=1}^{N_k} \rho_{k\ell} h_{m,k\ell} \right) s_b(t) + \omega''(t) \right\} \mathbb{I}(\mathcal{C}_3), \end{cases} \quad (12)$$

where

$$\begin{aligned} \mathcal{C}_1: & t_b \leq t < t_{b_m}, \\ \mathcal{C}_2: & t_{b_m} + (n_m - 1)t_m \leq t < t_{b_m} + n_m t_m, \forall n_m, \\ \mathcal{C}_3: & t_{b_m} \leq t < t_{b+1}. \end{aligned}$$

Herein, η denotes the optical-to-electrical coefficient, $\rho_{k\ell}$ indicates the RIS reflection coefficient, and $t_m = L_m/(N_m V_{\text{HST}})$ indicates the service time span of the n_m 'th RIS cell. Furthermore, $\omega(t) \sim \mathcal{N}(0, \sigma_\omega^2)$, $\omega'(t) \sim \mathcal{N}(0, \sigma_{\omega'}^2)$, and $\omega''(t) \sim \mathcal{N}(0, \sigma_{\omega''}^2)$ are additive white Gaussian noise terms.

III. PERFORMANCE ANALYSES

Through this section, the proposed network's average SNR and outage probability are formulated.

A. Average SNR

If we assume the RIS-assisted channels are mutually uncorrelated, the SNR of the b th FSO-BS link is obtained as

$$\gamma_b(t) = \begin{cases} \bar{\gamma}_b(h_b(t))^2 \mathbb{I}(\mathcal{C}_1), \\ \text{FOR: } \left\{ \sum_{\ell=1}^{N_\ell} \sum_{k=1}^{N_k} \bar{\gamma}_{k\ell} h_{m,k\ell}^2 \right\} \mathbb{I}(\mathcal{C}_2), \\ \text{DOR: } \left\{ \sum_{n_m=1}^{N_m} \sum_{\ell=1}^{N_\ell} \sum_{k=1}^{N_k} \bar{\gamma}'_{k\ell} h_{m,k\ell}^2 \right\} \mathbb{I}(\mathcal{C}_3), \end{cases} \quad (13)$$

wherein we have $\bar{\gamma}_b = \eta^2 P / \sigma_\omega^2$, $\bar{\gamma}_{k\ell} = \eta^2 \rho_{k\ell}^2 P / \sigma_{\omega'}^2$, and $\bar{\gamma}'_{k\ell} = \eta^2 \rho_{k\ell}^2 P / \sigma_{\omega''}^2$. Thus, the average SNR is achieved by replacing $(h_b(t))^2$ and $h_{m,k\ell}^2$ with $\Gamma_b^2(t) = \mathbb{E}\{(h_b(t))^2\}$ and $\Gamma_{m,k\ell}^2 = \mathbb{E}\{h_{m,k\ell}^2\}$ in (13), respectively. Under the weak turbulence, by the use of (6) and (10), we have

$$\begin{aligned} \Gamma_{m,k\ell}^2 &\cong \frac{\sqrt{\varpi_{k\ell}} C_b^3}{8\sqrt{\pi} C_a^{\varpi_{k\ell}}} \left[\frac{(5 - \ln(C_a))}{3} \left(\frac{e^{-C_g^2} (C_g^2 + 1)}{\sqrt{\pi} C_g^3} - \operatorname{erfc}(C_g) \right) \right. \\ &\quad \left. + \frac{\sqrt{8\sigma_{k\ell}^2} C_b^{\varpi_{k\ell}}}{\sqrt{\pi} (\varpi_{k\ell} + 3)} \left(\frac{1}{\sqrt{\pi} C_g^{\varpi_{k\ell} + 3}} \Gamma\left(\frac{\varpi_{k\ell} + 4}{2}, C_g^2\right) - \operatorname{erfc}(C_g) \right) \right], \end{aligned} \quad (14a)$$

$$\Gamma_b^2(t) = \frac{\xi^2 (C_e/C_h)^{\xi^2+2} C_f}{2(\xi^2+2) C_d^{\xi^2}}$$

¹We assume that time shifts between the transmitted and received direct or RIS-assisted signals are ignitable thanks to short-range but high-rate links.

$$\times \left[\frac{1}{\sqrt{\pi}} \Gamma\left(\frac{\xi^2+3}{2}, C_h^2\right) - C_h^{\xi^2+2} \operatorname{erfc}(C_h) \right], \quad (14b)$$

where $C_g = \frac{C_b}{C_a \sqrt{8\sigma_{k\ell}^2}}$, and $C_h = \frac{C_e}{C_d \sqrt{8\sigma_{k\ell}^2}}$. However, under the moderate-to-strong turbulence, by using (7) and (11), we have

$$\Gamma_{m,k\ell}^2 = \frac{\sqrt{\varpi_{k\ell}\zeta}}{2\sqrt{\pi}\Gamma(\alpha_{k\ell})\Gamma(\beta_{k\ell})} \left(\frac{\alpha_{k\ell}\beta_{k\ell}}{C_a} \right)^{C_c} \times G_{2,4}^{4,1} \left(\frac{\alpha_{k\ell}\beta_{k\ell}}{C_a} \middle| \begin{matrix} -1-C_c, 1+\varpi_{k\ell} \\ -2-C_c, 1+C_c, \alpha_{k\ell}, \beta_{k\ell} \end{matrix} \right), \quad (15a)$$

$$\Gamma_b^2(t) = \frac{\xi^2}{\Gamma(\alpha_b)\Gamma(\beta_b)} \left(\frac{\alpha_b\beta_b}{C_d} \right)^{\xi^2} \times G_{2,4}^{4,1} \left(\frac{\alpha_b\beta_b}{C_d} \middle| \begin{matrix} -1-\xi^2, 1+\xi^2 \\ -2-\xi^2, \xi^2, \alpha_b, \beta_b \end{matrix} \right). \quad (15b)$$

B. Outage Probability

The QoS is ensured by keeping $\gamma_b(t)$ above a given threshold γ_{th} at time t . Therefore, the network's outage probability is defined as [20]

$$P_{out}(t) \triangleq \Pr\{\gamma_b(t) \leq \gamma_{th}\} = F_{\gamma_b(t)}(\gamma_b(t) = \gamma_{th}), \quad (16)$$

where $F_{\gamma_b(t)}(\gamma_b(t))$ shows the cumulative distribution function (CDF) of $\gamma_b(t)$, which is derived in the following theorems.

Theorem 4. *The CDF of $\gamma_b(t)$ under the weak turbulence is obtained for the direct and RIS-assisted FSO channels, as what follows.*

- *Direct FSO channels;*

$$F_{\gamma_b(t)}(\gamma_b(t)) = \frac{(C_e/C_h)^{\frac{\xi^2}{2}} C_f}{4 C_d^{\xi^2}} \times \left\{ \hat{C}_h^{\frac{\xi^2}{2}} \left[1 + \frac{\gamma_b(t)}{C_e} \right]^{\frac{\xi^2}{2}} \operatorname{erfc}\left(\hat{C}_h \left[1 + \frac{\gamma_b(t)}{C_e} \right]\right) - \frac{1}{\sqrt{\pi}} \Gamma\left(\frac{\xi^2+2}{4}, \hat{C}_h^2 \left[1 + \frac{\gamma_b(t)}{C_e} \right]^2\right) \right\} \mathbb{I}(C_1), \quad (17)$$

- *RIS-assisted FSO channels and the FOR scenario;*

$$F_{\gamma_b(t)}(\gamma_b(t)) = \prod_{\ell=1}^{N_\ell} \prod_{k=1}^{N_k} \frac{\sqrt{8\sigma_{k\ell}^2} (C_b/C_g)^{\frac{\varpi_{k\ell}}{2}}}{8\pi \sqrt{\varpi_{k\ell}} C_a^{\varpi_{k\ell}}} \times \left\{ \hat{C}_g^{\frac{\varpi_{k\ell}}{2}} \left[1 + \frac{\gamma_b(t)}{C_b} \right]^{\frac{\varpi_{k\ell}}{2}} \operatorname{erfc}\left(\hat{C}_g \left[1 + \frac{\gamma_b(t)}{C_b} \right]\right) - \frac{1}{\sqrt{\pi}} \Gamma\left(\frac{\varpi_{k\ell}+2}{4}, \hat{C}_g^2 \left[1 + \frac{\gamma_b(t)}{C_b} \right]^2\right) \right\} \mathbb{I}(C_2), \quad (18)$$

- *RIS-assisted FSO channels and the DOR scenario;*

$$F_{\gamma_b(t)}(\gamma_b(t)) = \prod_{m=1}^{N_m} \prod_{\ell=1}^{N_\ell} \prod_{k=1}^{N_k} \frac{\sqrt{8\sigma_{k\ell}^2} (C_b/C_g)^{\frac{\varpi_{k\ell}}{2}}}{8\pi \sqrt{\varpi_{k\ell}} C_a^{\varpi_{k\ell}}} \times \left\{ \hat{C}_g^{\frac{\varpi_{k\ell}}{2}} \left[1 + \frac{\gamma_b(t)}{C_b} \right]^{\frac{\varpi_{k\ell}}{2}} \operatorname{erfc}\left(\hat{C}_g \left[1 + \frac{\gamma_b(t)}{C_b} \right]\right) - \frac{1}{\sqrt{\pi}} \Gamma\left(\frac{\varpi_{k\ell}+2}{4}, \hat{C}_g^2 \left[1 + \frac{\gamma_b(t)}{C_b} \right]^2\right) \right\} \mathbb{I}(C_3), \quad (19)$$

where $\hat{C}_h = C_h/\sqrt{\gamma_b}$, $\hat{C}_g = C_g/\sqrt{\gamma_{k\ell}}$, and $\hat{C}_g = C_g/\sqrt{\gamma_{k\ell}^t}$.

Proof. See Appendix D.

Theorem 5. *The CDF of $\gamma_b(t)$ under the moderate-to-strong turbulence is obtained for the direct and RIS-assisted FSO channels, as what follows.*

- *Direct FSO channels;*

$$F_{\gamma_b(t)}(\gamma_b(t)) = \frac{\xi^2}{\bar{\gamma}_b^{\frac{\xi^2}{2}} \Gamma(\alpha_b)\Gamma(\beta_b)} \left(\frac{\alpha_b\beta_b}{C_d} \right)^{\xi^2} \times G_{2,4}^{4,1} \left(\frac{\alpha_b\beta_b\sqrt{\gamma_b(t)}}{\sqrt{\gamma_b} C_d} \middle| \begin{matrix} 1-\xi^2, 1+\xi^2 \\ -\xi^2, \xi^2, \alpha_b, \beta_b \end{matrix} \right) \mathbb{I}(C_1), \quad (20)$$

- *RIS-assisted FSO channels and the FOR scenario;*

$$F_{\gamma_b(t)}(\gamma_b(t)) = \prod_{\ell=1}^{N_\ell} \prod_{k=1}^{N_k} \frac{\sqrt{\varpi_{k\ell}\zeta}}{\sqrt{\pi} \bar{\gamma}_{k\ell}^{\frac{C_c}{2}} \Gamma(\alpha_{k\ell})\Gamma(\beta_{k\ell})} \left(\frac{\alpha_{k\ell}\beta_{k\ell}}{C_a} \right)^{C_c} \times G_{2,4}^{4,1} \left(\frac{\alpha_{k\ell}\beta_{k\ell}\sqrt{\gamma_b(t)}}{\sqrt{\gamma_{k\ell}} C_a} \middle| \begin{matrix} 1-C_c, 1+\varpi_{k\ell} \\ -C_c, 1+C_c, \alpha_{k\ell}, \beta_{k\ell} \end{matrix} \right) \mathbb{I}(C_2), \quad (21)$$

- *RIS-assisted FSO channels and the DOR scenario;*

$$F_{\gamma_b(t)}(\gamma_b(t)) = \prod_{m=1}^{N_m} \prod_{\ell=1}^{N_\ell} \prod_{k=1}^{N_k} \frac{\sqrt{\varpi_{k\ell}\zeta}}{\sqrt{\pi} \bar{\gamma}_{k\ell}^{\frac{C_c}{2}} \Gamma(\alpha_{k\ell})\Gamma(\beta_{k\ell})} \left(\frac{\alpha_{k\ell}\beta_{k\ell}}{C_a} \right)^{C_c} \times G_{2,4}^{4,1} \left(\frac{\alpha_{k\ell}\beta_{k\ell}\sqrt{\gamma_b(t)}}{\sqrt{\gamma_{k\ell}} C_a} \middle| \begin{matrix} 1-C_c, 1+\varpi_{k\ell} \\ -C_c, 1+C_c, \alpha_{k\ell}, \beta_{k\ell} \end{matrix} \right) \mathbb{I}(C_3). \quad (22)$$

Proof. See Appendix E.

IV. NUMERICAL RESULTS AND DISCUSSIONS

In this section, we firstly analyze the network's performance under the assumed serving scenarios and compare the proposed RIS-assisted systems with the existing relay-based ones from the average SNR and outage probability perspectives. The system model parameters used for numerical results are summarized in Table I. Then, we provide a system design framework with an illustrative sample for practical use cases.

A. Results and Discussions

In Fig. 3, we show that there exists an optimal value of L_0 by plotting the average SNR over an assumed 1 [km] distance between two adjacent FSO-BSSs. For the considered conditions, we observe that $L_0 \simeq 8$ is optimal for all scenarios.

Fig. 4 depicts the network's outage probability versus the average SNR for the two considered turbulence conditions. In this figure, we compare the performances of the proposed systems based on the FOR and DOR scenarios with traditional relay systems. All results are compared with 500-iteration Monte-Carlo simulations. It is shown that the DOR scenario offers the highest performance compared to the others, where the FOR scenario decreases the network's outage probability with respect to the relay system. The reason is that, in the DOR scenario, the incident FSO beams at all elements of every RIS are reflected in a concentrated direction, which boosts the received signal power at the HST's detector. However,

TABLE I
SYSTEM PARAMETERS FOR NUMERICAL RESULTS.

Parameter	Symbol	Value
Vertical distance along the track	L_d	2.5 [m]
Half divergence angle	Ψ	3.5°
RIS setup	(N_k, N_ℓ, N_m)	(10, 10, 25)
RIS reflection coefficient (passive)	$\rho_{k\ell}$	0.95
Attenuation factor	γ	0.44 [dB/km]
Refraction structure index	C_n^2	10^{-15} [m ^{-2/3}]
Wavelength	λ	850 [nm]
Source beam waist	\hat{w}_0	$\lambda/2\pi\Psi$
Building sway fluctuations	$\delta_s, \delta_r, \delta_l$	5
Detector diameters	(α_r, α_p)	(2.5, 20)[cm]
Approximation factor	ζ	100
Misalignment parameters	$(h_{0,b}, \xi)$	(0.0764, 2.35)
Optical transmission power	P	40 [mW]
Optical-to-electrical coefficient	η	0.5
Speed of the HST	V_{HST}	300 [km/h]
Additive noise standard deviations	$\sigma_\omega, \sigma_{\omega'}, \sigma_{\omega''}$	10^{-7} [A/Hz]

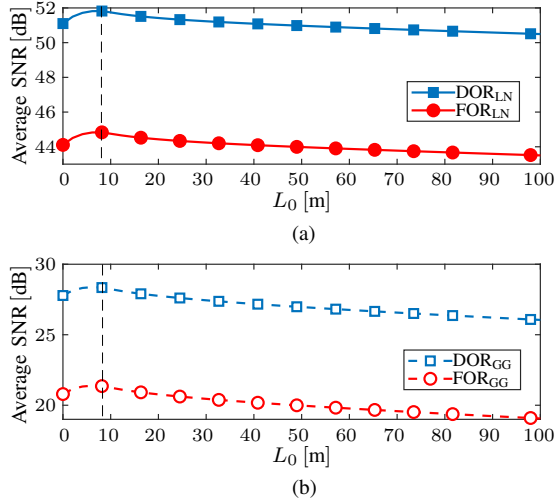


Fig. 3. The average SNR over the assumed 1 [km] distance between two adjacent FSO-BSs versus L_0 for (a) weak turbulence and (b) moderate-to-strong turbulence conditions.

in the FOR scenario, the incident FSO beams at each RIS cell are reflected in a dedicated direction, independent of the direction of other cells. Conventionally, we assume that only a limited number of RIS elements reflect the incident FSO beams in one direction in the case of the relay system. If we assume to have a generic passive FSO detector and transmitter instead of each RIS, the number of RIS elements required for simulating the detector's aperture is $(\alpha_p/\alpha_r)^2$. Finally, it is verified that all systems have lower outage probabilities under weak turbulence conditions as opposed to the moderate-to-strong ones. As clearly observed from Fig. 4, our derived closed-form formulas provide an identical match to simulation results. This conclusion is extendable to the rest of the figures.

Fig. 5 illustrates the diameters of the coverage areas served

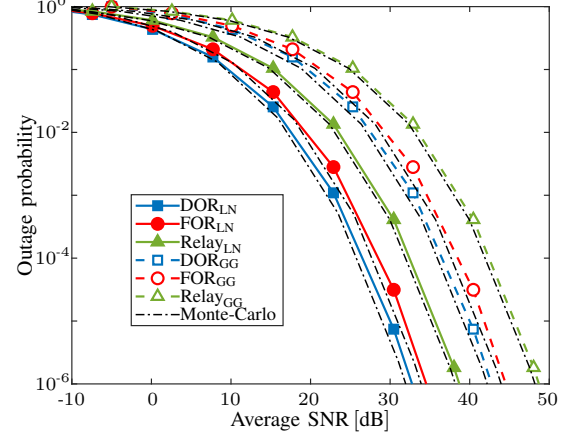


Fig. 4. The network's outage probability versus the average SNR for different coverage scenarios and turbulence conditions.

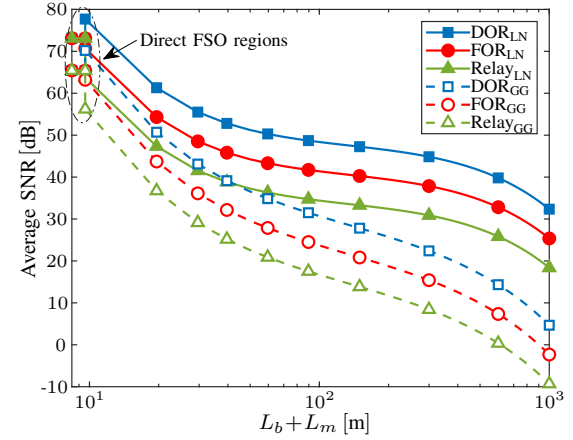


Fig. 5. The average SNR versus the coverage diameter for different coverage scenarios and turbulence conditions.

by the proposed access systems under the two considered turbulence conditions. In this regard, the average SNR at the HST's detector is plotted versus $L_b + L_m$ for the sample b th FSO-BS. It is shown that the DOR scenario extends the coverage area with respect to both FOR and traditional relay systems. Besides, the FOR scenario offers a wider coverage area compared to the relay system. In detail, for the average SNR of 30 [dB], the diameter of the coverage area offered by the DOR scenario is 60% and 304%, under the weak turbulence, and 145% and 277%, under the moderate-to-strong turbulence, larger than those of the FOR and relay systems, respectively. By increasing the coverage area served by each FSO-BS and its paired RIS, the numbers of required FSO-BSs and handovers decrease for a fixed railway distance. The dotted area in Fig. 5 depicts the region directly covered by the b th FSO-BS with the diameter of L_b . It is inferred that, contrary to the FOR and relay systems, the DOR scenario results in higher average SNR at the end of L_b and beginning of L_m , thanks to concentrating all dispersed beams on one point. The results of Fig. 5 verify that the assumed distance between two adjacent FSO-BSs for plotting Fig. 3 is feasible.

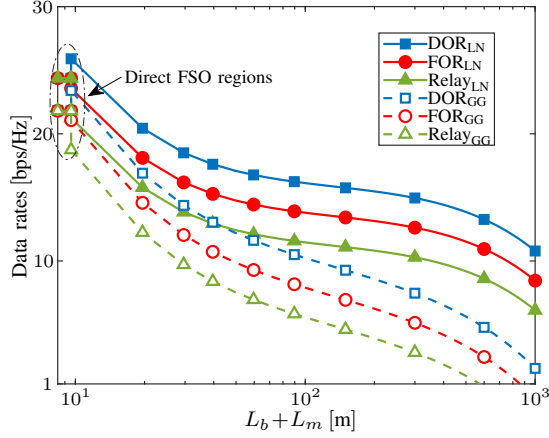


Fig. 6. The network's achievable data rates versus the coverage diameter for different coverage scenarios and turbulence conditions.

Fig. 6 presents the network's achievable data rates versus the diameters of the coverage areas. This figure's attribute is similar to that of Fig. 5 under different serving scenarios and turbulence conditions. Concretely, the DOR scenario averagely offers 16% and 45% higher data rates with respect to the FOR and relay systems, respectively, under weak turbulence conditions. Likewise, under moderate-to-strong conditions, the DOR scenario sequentially provides 26% and 63% higher data rates compared to the FOR and relay systems. Meanwhile, the coverage analyses for Fig. 5 can be easily applied for Fig. 6.

Fig. 7 depicts the average SNR versus the coverage diameter and a new analysis dimension, the RIS size. It is revealed that increasing the number of RIS elements, i.e., $N_k \times N_\ell \times N_m$, would monotonically raise the average SNR for a given coverage diameter. However, the average SNR becomes saturated for gigantic RIS sizes. For plotting this figure, it is assumed that the divergence angle is adjusted based on the RIS size. The reason is that the incident FSO beam from every FSO-BS must cover the whole area of the paired RIS. In other words, the larger RIS sizes, the wider divergence angles, hence more expensive FSO expanders are required.

B. System Design Framework

A system design framework for practical deployments is suggested here by taking advantage of the provided numerical results and discussions. To this end, we set the outage probability at the HST receiver to be 10^{-3} . According to Fig. 4, the required SNR value for each scenario and turbulence condition is deduced. Then, the diameter of the coverage area supported by each FSO-BS and the achievable data rates at the HST are found in Fig. 5 and Fig. 6, respectively. Table II summarizes the proposed design parameters for the assumed railway length of 100 [km].

Fig. 8 shows the number of needed FSO-BSs for the assumed railway setup under different scenarios and turbulence conditions, as given in Table II. It is verified that the DOR strategy requires much simpler infrastructures with less handover frequency compared to the other systems, at the cost of demanding a train tracking procedure. In addition, the

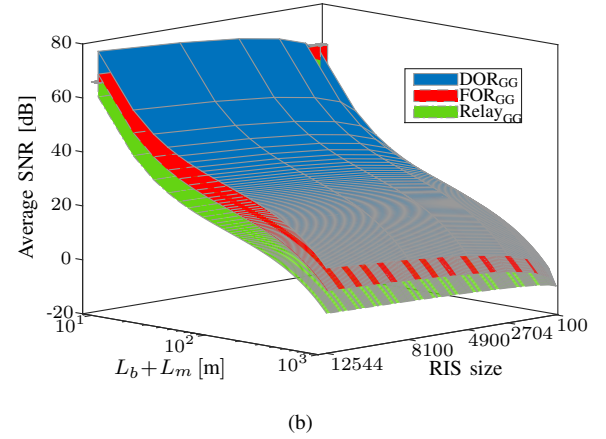
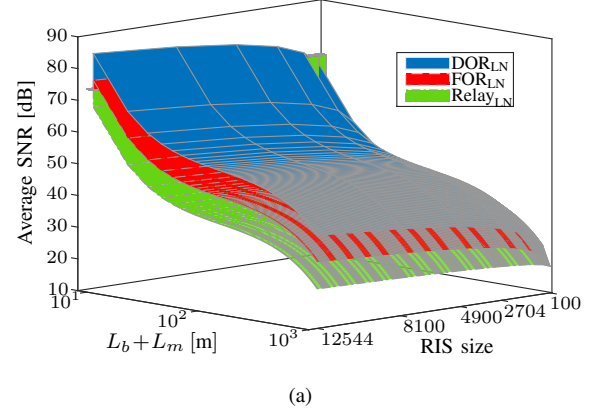


Fig. 7. The average SNR versus the coverage diameter and RIS size under (a) weak turbulence and (b) moderate-to-strong turbulence FSO channels.

TABLE II
A SYSTEM DESIGN SAMPLE.

	FOR		DOR		Relay	
	LN	GG	LN	GG	LN	GG
P_{out}	10^{-3}					
Required SNR [dB]	25	35	22	33	27	37
$L_b + L_m$ [m]	1000	28	1130	88	325	20
Number of FSO-BSs (B)*	100	3572	89	114	308	5000

*It is assumed that the length of the railway line is 100 [km].

FOR strategy requires fewer FSO-BSs, hence fewer handover processes, with respect to the traditional relay system.

V. CONCLUSION

In this paper, we proposed a novel FSO access setup based on the RIS technology to enhance the performance of the existing access networks which provide broadband Internet access for HSTs. We firstly derived the statistical expressions of direct and RIS-assisted FSO channels under weak and moderate-to-strong fading conditions. Then, the average SNR and outage probability formulas at the HST were computed for the FOR and DOR coverage scenarios. Through the numerical results, it was shown that the proposed access network offers

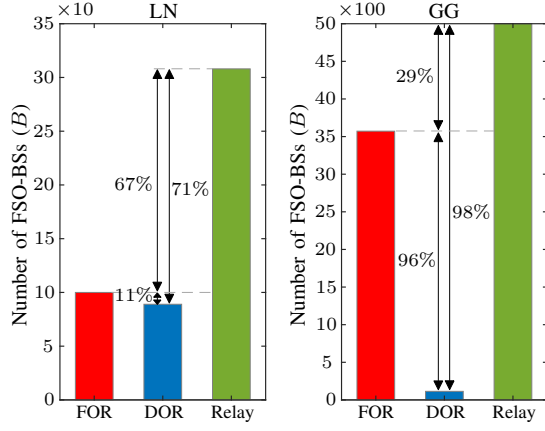


Fig. 8. The number of the required FSO-BSs for the assumed railway length of 100 [km].

up to around 44% higher data rates and 240% wider coverage area served by each FSO-BS compared to the relay-assisted alternative. The increase of the FSO-BS coverage on average reduces 67% the number of FSO-BSs required to support a given railway distance. Decreasing the number of FSO-BSs in an access network would decrease the handover frequency and CAPEX, as well. The main results were verified by Monte-Carlo simulations. Finally, a system design framework for practical deployments was suggested based on the achieved results and assumed design sample. The calculated values on the design table verified our results that the proposed setup boosts the performances of the existing alternatives.

APPENDIX A PROOF OF THEOREM 1

Using (4) and [38, Eq. (12)], the p.d.f of h_{kl} is obtained as

$$\begin{aligned}
 f_{h_{kl}}(h_{kl}) &= \int f_{h_{kl}|h_{t,kl}}(h_{kl}|h_{t,kl}) f_{h_{t,kl}}(h_{t,kl}) dh_{t,kl} \\
 &= \int_{\frac{h_{kl}}{C_a}}^{\infty} \frac{1}{h_{p,kl} h_{t,kl}} f_{h_{g,kl}}\left(\frac{h_{kl}}{h_{p,kl} h_{t,kl}}\right) f_{h_{t,kl}}(h_{t,kl}) dh_{t,kl} \\
 &= \frac{\sqrt{\varpi_{kl}}}{2\sqrt{\pi} h_{kl}} \left(\frac{h_{kl}}{C_a}\right)^{\varpi_{kl}} \\
 &\quad \times \int_{\frac{h_{kl}}{C_a}}^{\infty} \left[\ln\left(\frac{C_a h_{t,kl}}{h_{kl}}\right)\right]^{-1/2} \frac{1}{h_{t,kl}^{\varpi_{kl}}} f_{h_{t,kl}}(h_{t,kl}) dh_{t,kl}, \quad (23)
 \end{aligned}$$

where $C_a = h_{0,kl} h_{p,kl}$. Now, by inserting (2) for the weak turbulence into (23) and some mathematical manipulations, (6) is achieved.

APPENDIX B PROOF OF THEOREM 2

By applying the same technique as in (23) and using (2) for the moderate-to-strong turbulence, we have

$$\begin{aligned}
 f_{h_{kl}}(h_{kl}) &= \frac{\sqrt{\varpi_{kl}}}{\sqrt{\pi} h_{kl}} \frac{(\alpha_{kl} \beta_{kl})^{\frac{\alpha_{kl} + \beta_{kl}}{2}}}{\Gamma(\alpha_{kl}) \Gamma(\beta_{kl})} \left(\frac{h_{kl}}{C_a}\right)^{\varpi_{kl}} \\
 &\quad \times \int_{\frac{h_{kl}}{C_a}}^{\infty} \left[\ln\left(\frac{C_a h_{t,kl}}{h_{kl}}\right)\right]^{-1/2} h_{t,kl}^{-\varpi_{kl}-1}
 \end{aligned}$$

$$\times h_{t,kl}^{\frac{1}{2}(\alpha_{kl} + \beta_{kl})} K_{\alpha_{kl} - \beta_{kl}} \left(2\sqrt{\alpha_{kl} \beta_{kl} h_{t,kl}}\right) dh_{t,kl} \quad (24a)$$

$$\begin{aligned}
 &= \frac{\sqrt{\varpi_{kl}}}{2\sqrt{\pi} h_{kl}} \frac{(\alpha_{kl} \beta_{kl})^{\varpi_{kl}}}{\Gamma(\alpha_{kl}) \Gamma(\beta_{kl})} \left(\frac{h_{kl}}{C_a}\right)^{\varpi_{kl}} \\
 &\quad \times \int_{\frac{h_{kl}}{C_a}}^{\infty} \left[\ln\left(\frac{C_a h_{t,kl}}{\alpha_{kl} \beta_{kl} h_{kl}}\right)\right]^{-1/2} h_{t,kl}^{-\varpi_{kl}-1} \\
 &\quad \times G_{0,2}^{2,0} \left(h_{t,kl} \mid \alpha_{kl}, \beta_{kl}\right) dh_{t,kl} \quad (24b)
 \end{aligned}$$

$$\begin{aligned}
 &\cong \frac{\sqrt{\varpi_{kl} \zeta}}{2\sqrt{\pi} h_{kl}} \frac{(\alpha_{kl} \beta_{kl})^{\varpi_{kl}}}{\Gamma(\alpha_{kl}) \Gamma(\beta_{kl})} \left(\frac{h_{kl}}{C_a}\right)^{\varpi_{kl}} \left(\frac{\alpha_{kl} \beta_{kl} h_{kl}}{C_a}\right)^{1/2\zeta-1} \\
 &\quad \times \int_{\frac{h_{kl}}{C_a}}^{\infty} \left[h_{t,kl} - \frac{\alpha_{kl} \beta_{kl} h_{kl}}{C_a}\right]^{-1/2\zeta} h_{t,kl}^{-\varpi_{kl}-1} \\
 &\quad \times G_{0,2}^{2,0} \left(h_{t,kl} \mid \alpha_{kl}, \beta_{kl}\right) dh_{t,kl}, \quad (24c)
 \end{aligned}$$

where $C_c = 1/2\zeta + \varpi_{kl} - 1$. Next, (7) is obtained after some mathematical computations. Note that, to derive (24b) and solve (24c), the similar steps as in [39, Eq. (5)] and [39, Eq. (6)] are passed, respectively. In addition, to derive (24c), we utilize the approximation $\ln(x) \cong \zeta x^{1/\zeta} - \zeta$, for the large enough ζ .

APPENDIX C PROOF OF THEOREM 3

Similar to (23), the p.d.f of $h_b(t)$ is obtained as

$$\begin{aligned}
 f_{h_b(t)}(h_b(t)) &= \frac{\xi^2 (h_b(t))^{\xi^2-1}}{C_d^{\xi^2}} \\
 &\quad \times \int_{\frac{h_b(t)}{C_d}}^{\infty} (h_{t,b}(t))^{-\xi^2} f_{h_{t,b}(t)}(h_{t,b}(t)) dh_{t,b}(t) \quad (25a)
 \end{aligned}$$

$$\begin{aligned}
 &= \frac{\xi^2 (h_b(t))^{\xi^2-1}}{C_d^{\xi^2}} \frac{2(\alpha_b \beta_b)^{\frac{1}{2}(\alpha_b + \beta_b)}}{\Gamma(\alpha_b) \Gamma(\beta_b)} \int_{\frac{h_b(t)}{C_d}}^{\infty} (h_{t,b}(t))^{-\xi^2-1} \\
 &\quad \times (h_{t,b}(t))^{\frac{1}{2}(\alpha_b + \beta_b)} K_{\alpha_b - \beta_b} \left(2\sqrt{\alpha_b \beta_b h_{t,b}(t)}\right) dh_{t,b}(t) \quad (25b) \\
 &= \frac{\xi^2 (h_b(t))^{\xi^2-1}}{C_d^{\xi^2}} \frac{(\alpha_b \beta_b)^{\xi^2}}{\Gamma(\alpha_b) \Gamma(\beta_b)} \\
 &\quad \times \int_{\frac{h_b(t)}{C_d}}^{\infty} (h_{t,b}(t))^{-\xi^2-1} G_{0,2}^{2,0} \left(h_{t,b}(t) \mid \alpha_b, \beta_b\right) dh_{t,b}(t). \quad (25c)
 \end{aligned}$$

Then, (11) is achieved after some mathematical manipulations.

APPENDIX D PROOF OF THEOREM 4

We firstly derive the p.d.f of $\gamma_b(t)$ then compute its corresponding CDF. In this regard, we define $\gamma_{m,kl} \triangleq \bar{\gamma}_{kl} h_{m,kl}^2$ and $\gamma'_{m,kl} \triangleq \bar{\gamma}'_{kl} h_{m,kl}^2$. Besides, we know that the RIS-assisted channels are uncorrelated, hence independent. Thus, we have

$$\begin{aligned}
 f_{\gamma_b(t)}(\gamma_b(t)) &= f_{\bar{\gamma}_b(h_b(t))^2}(\bar{\gamma}_b(h_b(t))^2) \\
 &= \frac{\xi^2 (\gamma_b(t))^{\frac{\xi^2}{2}-1} C_f}{4\bar{\gamma}_b^{\frac{\xi^2}{2}} C_d^{\xi^2}} \operatorname{erfc} \left(\frac{0.5 \ln \left(\frac{\gamma_b(t)}{\bar{\gamma}_b C_d^2} \right) + C_e}{\sqrt{8\sigma_b^2}} \right) \mathbb{I}(C_1), \quad (26)
 \end{aligned}$$

for the direct FSO channels. Likewise, we have

$$\begin{aligned}
 f_{\gamma_b(t)}(\gamma_b(t)) &= \prod_{\ell=1}^{N_\ell} \prod_{k=1}^{N_k} f_{\gamma_{m,k\ell}}(\gamma_{m,k\ell}) \\
 &= \prod_{\ell=1}^{N_\ell} \prod_{k=1}^{N_k} \frac{\sqrt{\varpi_{k\ell}} \gamma_{m,k\ell}^{\frac{\varpi_{k\ell}}{2}-1}}{16\sqrt{\pi} \gamma_{k\ell}^{\frac{\varpi_{k\ell}}{2}} C_a^{\varpi_{k\ell}}} \operatorname{erfc} \left(\frac{0.5 \ln \left(\frac{\gamma_{m,k\ell}}{\gamma_{k\ell} C_a^2} \right) + C_b}{\sqrt{8\sigma_{k\ell}^2}} \right) \\
 &\quad \times \left\{ \left[\frac{(5 - \ln(C_a)) \gamma_{k\ell}^{\frac{\varpi_{k\ell}}{2}}}{\gamma_{m,k\ell}} + \frac{\sqrt{8\sigma_{k\ell}^2}}{\sqrt{\pi}} \right] \right. \\
 &\quad \times \exp \left(\frac{(0.5 \ln \left(\frac{\gamma_{m,k\ell}}{\gamma_{k\ell}} \right) + C_b)^2 - (0.5 \ln \left(\frac{\gamma_{m,k\ell}}{\gamma_{k\ell}} \right) + 2\sigma_{k\ell}^2)^2}{8\sigma_{k\ell}^2} \right) \\
 &\quad \left. + \left(\ln \left(\frac{\gamma_{m,k\ell}}{\gamma_{k\ell}} \right) + C_b \right) \exp \left(2\sigma_{k\ell}^2 \varpi_{k\ell} (1 + \varpi_{k\ell}) \right) \right\} \mathbb{I}(C_2), \quad (27)
 \end{aligned}$$

for the FOR RIS-assisted FSO channels, while

$$\begin{aligned}
 f_{\gamma_b(t)}(\gamma_b(t)) &= \prod_{n_m=1}^{N_m} \prod_{\ell=1}^{N_\ell} \prod_{k=1}^{N_k} f_{\gamma'_{m,k\ell}}(\gamma'_{m,k\ell}) \\
 &= \prod_{n_m=1}^{N_m} \prod_{\ell=1}^{N_\ell} \prod_{k=1}^{N_k} \frac{\sqrt{\varpi_{k\ell}} \gamma'_{m,k\ell}^{\frac{\varpi_{k\ell}}{2}-1}}{16\sqrt{\pi} \gamma_{k\ell}^{\frac{\varpi_{k\ell}}{2}} C_a^{\varpi_{k\ell}}} \operatorname{erfc} \left(\frac{0.5 \ln \left(\frac{\gamma'_{m,k\ell}}{\gamma_{k\ell} C_a^2} \right) + C_b}{\sqrt{8\sigma_{k\ell}^2}} \right) \\
 &\quad \times \left\{ \left[\frac{(5 - \ln(C_a)) \gamma_{k\ell}^{\frac{\varpi_{k\ell}}{2}}}{\gamma'_{m,k\ell}} + \frac{\sqrt{8\sigma_{k\ell}^2}}{\sqrt{\pi}} \right] \right. \\
 &\quad \times \exp \left(\frac{(0.5 \ln \left(\frac{\gamma'_{m,k\ell}}{\gamma_{k\ell}} \right) + C_b)^2 - (0.5 \ln \left(\frac{\gamma'_{m,k\ell}}{\gamma_{k\ell}} \right) + 2\sigma_{k\ell}^2)^2}{8\sigma_{k\ell}^2} \right) \\
 &\quad \left. + \left(\ln \left(\frac{\gamma'_{m,k\ell}}{\gamma_{k\ell}} \right) + C_b \right) \exp \left(2\sigma_{k\ell}^2 \varpi_{k\ell} (1 + \varpi_{k\ell}) \right) \right\} \mathbb{I}(C_3), \quad (28)
 \end{aligned}$$

for the DOR RIS-assisted FSO channels. In (26)–(28), we utilize (6), (10), and (13). Now, (17)–(19) are obtained from (26)–(28) pairwise by the use of the conventional CDF formula and the linearity property of integrals.

APPENDIX E PROOF OF THEOREM 5

Similar to Appendix D, the p.d.f expressions are as follows

$$\begin{aligned}
 f_{\gamma_b(t)}(\gamma_b(t)) &= \frac{\xi^2 (\gamma_b(t))^{\frac{\xi^2}{2}-1}}{2\bar{\gamma}_b^{\frac{\xi^2}{2}} \Gamma(\alpha_b) \Gamma(\beta_b)} \left(\frac{\alpha_b \beta_b}{C_d} \right)^{\xi^2} \\
 &\quad \times G_{1,3}^{3,0} \left(\frac{\alpha_b \beta_b \sqrt{\gamma_b(t)}}{\sqrt{\bar{\gamma}_b} C_d} \middle| \begin{matrix} 1+\xi^2 \\ \xi^2, \alpha_b, \beta_b \end{matrix} \right) \mathbb{I}(C_1), \quad (29)
 \end{aligned}$$

for the direct FSO channels. Besides, we have

$$\begin{aligned}
 f_{\gamma_b(t)}(\gamma_b(t)) &= \prod_{\ell=1}^{N_\ell} \prod_{k=1}^{N_k} \frac{\sqrt{\varpi_{k\ell}} \zeta \gamma_{m,k\ell}^{\frac{C_c}{2}-1}}{2\sqrt{\pi} \gamma_{k\ell}^{\frac{C_c}{2}} \Gamma(\alpha_{k\ell}) \Gamma(\beta_{k\ell})} \left(\frac{\alpha_{k\ell} \beta_{k\ell}}{C_a} \right)^{C_c} \\
 &\quad \times G_{1,3}^{3,0} \left(\frac{\alpha_{k\ell} \beta_{k\ell} \sqrt{\gamma_{m,k\ell}}}{\sqrt{\gamma_{k\ell}} C_a} \middle| \begin{matrix} 1+\varpi_{k\ell} \\ 1+C_c, \alpha_{k\ell}, \beta_{k\ell} \end{matrix} \right) \mathbb{I}(C_2), \quad (30)
 \end{aligned}$$

for the FOR RIS-assisted FSO channels, and

$$\begin{aligned}
 f_{\gamma_b(t)}(\gamma_b(t)) &= \prod_{n_m=1}^{N_m} \prod_{\ell=1}^{N_\ell} \prod_{k=1}^{N_k} \frac{\sqrt{\varpi_{k\ell}} \zeta \gamma'_{m,k\ell}^{\frac{C_c}{2}-1}}{2\sqrt{\pi} \gamma_{k\ell}^{\frac{C_c}{2}} \Gamma(\alpha_{k\ell}) \Gamma(\beta_{k\ell})} \left(\frac{\alpha_{k\ell} \beta_{k\ell}}{C_a} \right)^{C_c} \\
 &\quad \times G_{1,3}^{3,0} \left(\frac{\alpha_{k\ell} \beta_{k\ell} \sqrt{\gamma'_{m,k\ell}}}{\sqrt{\gamma_{k\ell}} C_a} \middle| \begin{matrix} 1+\varpi_{k\ell} \\ 1+C_c, \alpha_{k\ell}, \beta_{k\ell} \end{matrix} \right) \mathbb{I}(C_3), \quad (31)
 \end{aligned}$$

for the DOR RIS-assisted FSO channels. Through (29)–(31), we apply (7), (11), and (13). Next, (20)–(22) are obtained from (29)–(31), respectively.

REFERENCES

- [1] J. Kim, M. Schmieder, M. Peter, H. Chung, S.-W. Choi, I. Kim, and Y. Han, "A comprehensive study on mmwave-based mobile hotspot network system for high-speed train communications," *IEEE Transactions on Vehicular Technology*, vol. 68, no. 3, pp. 2087–2101, 2018.
- [2] S. Fathi-Kazerooni, Y. Kaymak, R. Rojas-Cessa, J. Feng, N. Ansari, M. Zhou, and T. Zhang, "Optimal positioning of ground base stations in free-space optical communications for high-speed trains," *IEEE Transactions on Intelligent Transportation Systems*, vol. 19, no. 6, pp. 1940–1949, 2017.
- [3] H. S. Khallaf and M. Uysal, "Comprehensive study on UAV-based FSO links for high-speed train backhauling," *Applied Optics*, vol. 60, no. 27, pp. 8239–8247, 2021.
- [4] B. Ai, X. Cheng, T. Kürner, Z.-D. Zhong, K. Guan, R.-S. He, L. Xiong, D. W. Matolak, D. G. Michelson, and C. Briso-Rodriguez, "Challenges toward wireless communications for high-speed railway," *IEEE Transactions on Intelligent Transportation Systems*, vol. 15, no. 5, pp. 2143–2158, 2014.
- [5] M. Goller, "Application of GSM in high speed trains: measurements and simulations," *IEE Colloquium on Radiocommunications in Transportation*, 1995.
- [6] C.-X. Wang, A. Ghazal, B. Ai, Y. Liu, and P. Fan, "Channel measurements and models for high-speed train communication systems: A survey," *IEEE Communications Surveys & Tutorials*, vol. 18, no. 2, pp. 974–987, 2015.
- [7] M. Aguado, O. Onandi, P. Agustin, M. Higuero, and E. Taquet, "Wimax on rails," *IEEE Vehicular Technology Magazine*, vol. 3, no. 3, pp. 47–56, 2008.
- [8] M. Kowal, S. Kubal, P. Piotrowski, and R. J. Zieliński, "Operational characteristic of wireless WiMax and IEEE 802.11x systems in underground mine environments," *International Journal of Electronics and Telecommunications*, vol. 56, pp. 81–86, 2010.
- [9] R. Paudel, Z. Ghassemlooy, H. Le-Minh, and S. Rajbhandari, "Modelling of free space optical link for ground-to-train communications using a Gaussian source," *IET Optoelectronics*, vol. 7, no. 1, pp. 1–8, 2013.
- [10] R. Paudel, X. Tang, and Z. Ghassemlooy, "Laboratory demonstration of FSO ground-to-train communications with multiple base stations," in *IEEE International Symposium on Communication Systems, Networks & Digital Signal Processing*, pp. 1–6, 2016.
- [11] T. Han and N. Ansari, "RADIATE: Radio over fiber as an antenna extender for high-speed train communications," *IEEE Wireless Communications*, vol. 22, no. 1, pp. 130–137, 2015.
- [12] M. Taheri, N. Ansari, J. Feng, R. Rojas-Cessa, and M. Zhou, "Provisioning internet access using FSO in high-speed rail networks," *IEEE Network*, vol. 31, no. 4, pp. 96–101, 2017.
- [13] Q. Fan, N. Ansari, J. Feng, R. Rojas-Cessa, M. Zhou, and T. Zhang, "Reducing the number of FSO base stations with dual transceivers for next-generation ground-to-train communications," *IEEE Transactions on Vehicular Technology*, vol. 67, no. 11, pp. 11 143–11 153, 2018.
- [14] Q. Fan, M. Taheri, N. Ansari, J. Feng, R. Rojas-Cessa, M. Zhou, and T. Zhang, "Reducing the impact of handovers in ground-to-train free space optical communications," *IEEE Transactions on Vehicular Technology*, vol. 67, no. 2, pp. 1292–1301, 2017.
- [15] Y. Kaymak, R. Rojas-Cessa, J. Feng, N. Ansari, and M. Zhou, "On divergence-angle efficiency of a laser beam in free-space optical communications for high-speed trains," *IEEE Transactions on Vehicular Technology*, vol. 66, no. 9, pp. 7677–7687, 2017.

- [16] W. A. Mabrouk, M. Abdullah, and M. Gismalla, "Enhancement of link range for FSO ground to train communications using multiple transmitters concept," in *IEEE International Conference on Information Science and Communication Technology*, pp. 1–7, 2019.
- [17] N. Mohan, M. M. Abadi, Z. Ghassemlooy, S. Zvanovec, R. Hudson, and M. R. Bhatnagar, "Sectorised base stations for FSO ground-to-train communications," *IET Optoelectronics*, vol. 14, no. 5, pp. 312–318, 2020.
- [18] A. M. Abdalla, J. Rodriguez, I. Elfergani, and A. Teixeira, *Optical and Wireless Convergence for 5G Networks*. Wiley Online Library, 2020.
- [19] M. A. Khalighi and M. Uysal, "Survey on free space optical communication: A communication theory perspective," *IEEE Communications Surveys & Tutorials*, vol. 16, no. 4, pp. 2231–2258, 2014.
- [20] P. Agheli, H. Beyranvand, and M. J. Emadi, "UAV-assisted underwater sensor networks using RF and optical wireless links," *Journal of Lightwave Technology (Early Access)*, 2021.
- [21] H. Kaushal and G. Kaddoum, "Optical communication in space: Challenges and mitigation techniques," *IEEE Communications Surveys & Tutorials*, vol. 19, no. 1, pp. 57–96, 2016.
- [22] P. Agheli, M. J. Emadi, and H. Beyranvand, "Designing cost- and energy-efficient cell-free massive MIMO network with fiber and FSO fronthaul links," *AUT Journal of Electrical Engineering*, vol. 53, no. 2, pp. 4–4, 2021.
- [23] M. Safari and M. Uysal, "Relay-assisted free-space optical communication," *IEEE Transactions on Wireless Communications*, vol. 7, no. 12, pp. 5441–5449, 2008.
- [24] M. A. Kashani, M. M. Rad, M. Safari, and M. Uysal, "All-optical amplify-and-forward relaying system for atmospheric channels," *IEEE Communications Letters*, vol. 16, no. 10, pp. 1684–1687, 2012.
- [25] H. S. Khallaf and M. Uysal, "UAV-based FSO communications for high speed train backhauling," in *IEEE Wireless Communications and Networking Conference*, pp. 1–6, 2019.
- [26] X. Yuan, Y.-J. A. Zhang, Y. Shi, W. Yan, and H. Liu, "Reconfigurable-intelligent-surface empowered wireless communications: Challenges and opportunities," *IEEE Wireless Communications*, vol. 28, no. 2, pp. 136–143, 2021.
- [27] M. Najafi and R. Schober, "Intelligent reflecting surfaces for free space optical communications," in *IEEE Global Communications Conference*, pp. 1–7, 2019.
- [28] M. Najafi, B. Schmauss, and R. Schober, "Intelligent reflecting surfaces for free space optical communication systems," *IEEE Transactions on Communications*, vol. 69, no. 9, pp. 6134–6151, 2021.
- [29] A. R. Ndjiongue, T. Ngatched, O. Dobre, A. G. Armada, and H. Haas, "Analysis of RIS-based terrestrial-FSO link over GG turbulence with distance and jitter ratios," *Journal of Lightwave Technology (Early Access)*, 2021.
- [30] M. Najafi, V. Jamali, R. Schober, and H. V. Poor, "Physics-based modeling and scalable optimization of large intelligent reflecting surfaces," *IEEE Transactions on Communications*, vol. 69, no. 4, pp. 2673–2691, 2020.
- [31] H. Ajam, M. Naja, V. Jamali, and R. Schober, "Channel modeling for IRS-assisted FSO systems," in *IEEE Wireless Communications and Networking Conference*, pp. 1–7, 2021.
- [32] H. Jia, J. Zhong, M. N. Janardhanan, and G. Chen, "Ergodic capacity analysis for fso communications with uav-equipped irs in the presence of pointing error," in *IEEE International Conference on Communication Technology*, pp. 949–954, 2020.
- [33] L. Yang, W. Guo, and I. S. Ansari, "Mixed dual-hop FSO-RF communication systems through reconfigurable intelligent surface," *IEEE Communications Letters*, vol. 24, no. 7, pp. 1558–1562, 2020.
- [34] A. M. Abdelhady, A. K. S. Salem, O. Amin, B. Shihada, and M.-S. Alouini, "Visible light communications via intelligent reflecting surfaces: Metasurfaces vs mirror arrays," *IEEE Open Journal of the Communications Society*, vol. 2, pp. 1–20, 2020.
- [35] A. R. Ndjiongue, T. M. Ngatched, O. A. Dobre, and H. Haas, "Reconfigurable intelligent surface-based VLC receivers using tunable liquid-crystals: The concept," *Journal of Lightwave Technology*, vol. 39, no. 10, pp. 3193–3200, 2021.
- [36] M. Di Renzo, K. Ntontin, J. Song, F. H. Danufane, X. Qian, F. Lazarakis, J. De Rosny, D.-T. Phan-Huy, O. Simeone, R. Zhang *et al.*, "Reconfigurable intelligent surfaces vs. relaying: Differences, similarities, and performance comparison," *IEEE Open Journal of the Communications Society*, vol. 1, pp. 798–807, 2020.
- [37] E. Björnson, Ö. Özdogan, and E. G. Larsson, "Intelligent reflecting surface versus decode-and-forward: How large surfaces are needed to beat relaying?" *IEEE Wireless Communications Letters*, vol. 9, no. 2, pp. 244–248, 2019.
- [38] A. A. Farid and S. Hranilovic, "Outage capacity optimization for free-space optical links with pointing errors," *Journal of Lightwave Technology*, vol. 25, no. 7, pp. 1702–1710, 2007.
- [39] W. G. Alheadary, K.-H. Park, and M.-S. Alouini, "BER analysis of multi-hop heterodyne FSO systems with fixed gain relays over general Malaga turbulence channels," in *IEEE International Wireless Communications and Mobile Computing Conference*, pp. 1172–1177, 2017.